Materials and Design 164 (2019) 107555

Contents lists available at ScienceDirect

Materials and Design

journal homepage: www.elsevier.com/locate/matdes

Study of the influence of Zr on the mechanical properties and functional response of Ti-Nb-Ta-Zr-O alloy for orthopedic applications

Srijan Acharya, Arpana Gopi Panicker, Devara Vijaya Laxmi, Satyam Suwas, Kaushik Chatterjee *

Department of Materials Engineering, Indian Institute of Science, Bangalore 560012, India

HIGHLIGHTS

- A low modulus Ti-34Nb-2Ta-0.5O alloy with a microstructure similar to that of Ti-34Nb-2Ta-3Zr-0.5O was developed.
- The presence of oxygen stabilized β-phase and caused significant interstitial solid solution strengthening in both alloys.
- The difference in texture between the two alloys resulted in lower elastic modulus of Ti-34Nb-2Ta-0.5O.
- Presence of Zr in Ti-34Nb-2Ta-3Zr-0.5O improved both its tensile strength and corrosion resistance.
- In vitro studies with osteoblasts revealed good cellular response to both the alloys.

GRAPHICAL ABSTRACT

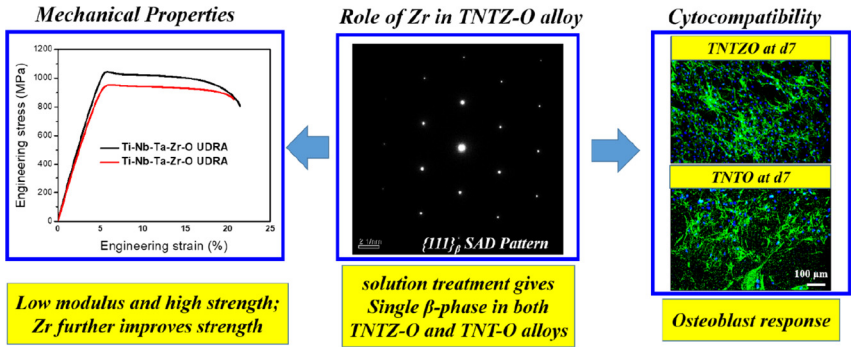

ARTICLE INFO

Article history:
Received 9 August 2018
Received in revised form 15 December 2018
Accepted 17 December 2018
Available online 19 December 2018

Keywords:
Titanium alloys
Biomaterials
Mechanical properties
Texture
Corrosion
Biocompatibility

ABSTRACT

In Ti-Nb-Ta-Zr based β-titanium alloys intended for orthopedic applications, Zr does not affect the stability of low modulus β-phase, unlike Nb and Ta. The present study attempts to investigate the influence of Zr on the overall mechanical and functional responses of a Ti-Nb-Ta-Zr-O alloy in contrast to a new Ti-Nb-Ta-O alloy. In each material, different crystallographic textures were produced by varying the processing route. While both alloys were found to show low elastic modulus values due to their β-only microstructures, Ti-Nb-Ta-O alloy had lower elastic modulus because of its favorable crystallographic orientation caused by absence of Zr. The tensile strength values were remarkably high for both due to the presence of interstitial oxygen. The hardening effect of Zr was also evident from the higher strength of Ti-Nb-Ta-Zr-O as compared to Ti-Nb-Ta-O alloy. Although the corrosion resistance and in vitro biological behavior of the two alloys were satisfactory, the Ti-Nb-Ta-Zr-O alloy showed lower corrosion rate and improved osteoblast attachment than the Ti-Nb-Ta-O alloy. Thus, whereas the two alloys show promising performance in terms of their mechanical and functional response, presence of Zr marginally improves the performance in the Ti-Nb-Ta-Zr-O for orthopedic applications.

1. Introduction

Metallic materials are widely used to prepare implants for the replacement of structural body parts that bear loads. One of the common causes of failure of metallic implants is stress shielding effect. This is caused by the mismatch in stiffness between the implant material (typically well above 100 GPa) and that of the human bone (~30 GPa). As a result, the cortical bone is shielded from the applied load by the implant leading to a loss of bone mass around the implants (osteopenia) and loosening of the implant leading to eventual failure [1]. Among the present alloy systems in use, Ti-based alloys have the lowest elastic moduli

* Corresponding author.
E-mail address: kchatterjee@iisc.ac.in (K. Chatterjee).

https://doi.org/10.1016/j.matdes.2018.107555

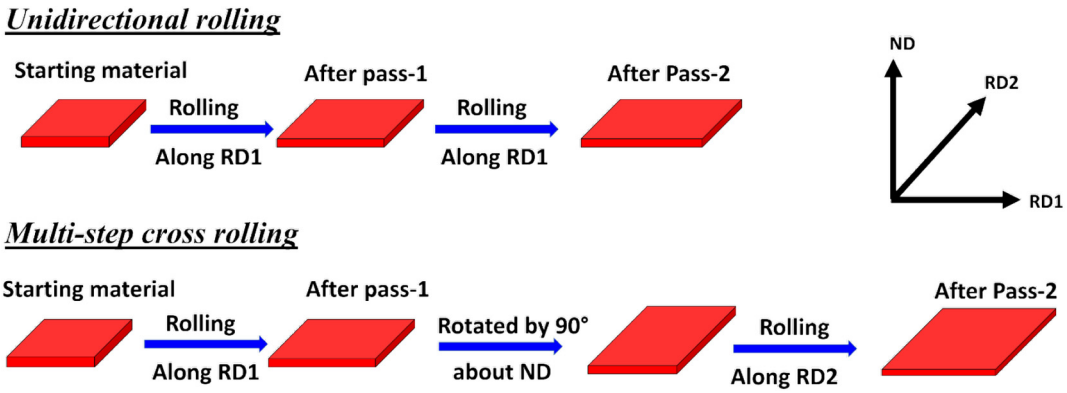

Fig. 1. Schematic showing the difference between the uniaxial (UDR) and multi-step cross-rolling (MSCR) processes; the direction of rolling is horizontal (along blue arrow); sample axes are also shown below. (For interpretation of the references to color in this figure legend, the reader is referred to the web version of this article.)

[2,3]. In addition, their biocompatibility has made them attractive materials for implants. However, the elastic modulus of α-titanium is still higher than that of human bones. Ti-alloys having only metastable β-phase possess lower elastic modulus, in comparison with currently used cp-Ti and Ti-6Al-4V which in general consists of α and α + β phases, respectively [4]. Therefore, attempts have been made to prepare β-titanium alloys with the addition of β-stabilizers in suitable amount. Certain β-stabilizers such as Nb and Ta have been found to be more effective in reducing the elastic modulus of β-phase [5–7], than others [8]. Most of the studies aimed at development of such alloys are based on having Nb as the primary alloying element [9–12]. Apart from β-stabilizers, neutral elements such as Zr and Sn have also been reported to be beneficial for achieving low elastic modulus [13,14]. However, to ensure a low modulus value, the concentrations of all these elements need to be maintained in a certain range. In this regard, one key parameter is the electron/atom (e/a) ratio, which must lie in the range of 4.20–4.24 to ensure lower modulus of β-phase [5]. Several Ti-Nb based compositions consisting of Ta, and Zr as additional alloying elements have been studied with maintaining this specific e/a ratio such as Ti-29Nb-13Ta-4.6Zr [6,15,16], Ti–35Nb–8Zr–5Ta [17,18], Ti–29Nb–9Ta–10Zr [19] and Ti–35.9Nb–2Ta–2.7Zr–0.3O [7,20–22], etc. These alloying elements, in addition to reducing the modulus in β alloy, also are found to be less cytotoxic than Al, V and Ni, etc. [1,23,24]. Therefore, these newly emerging classes of alloys are considered as potential candidates for replacing the current materials in use for enhanced performance of the device.

An implant material should ideally have high fatigue and wear resistance, which are associated with high mechanical strength of the material [25]. In spite of the potential showed by the low modulus β alloys, their mechanical strength remains a concern. Therefore, strengthening of these alloys is necessary in order to compete with the present alloys in use. The most common way to strengthen β titanium alloys is by aging. However, aging also increases the modulus by precipitating the second phases. Apart from aging treatment, the strength can also be improved by changing the composition to utilize solid solution strengthening or by work hardening or grain refinement. In the Ti-Nb-Ta-Zr alloys, increase in the strength through compositional changes can only be done such that the stability of the β phase is not compromised. In the Ti-Nb-Ta-Zr alloys, the absence of Zr does not change the e/a ratio unlike Nb and Ta. Zr is also a neutral element with respect to Ti whereas Nb and Ta are β stabilizers. However, the presence of Zr is found to retard the formation of other metastable phases such as ω or α″, which are detrimental for the properties of these alloys [26]. Zr has also been reported to improve corrosion resistance in Ti-Nb-Zr alloys [27,28]. In some of the recent studies, addition of oxygen in Ti-Nb-Ta-Zr alloys have been found to result in stabilizing the β phase, in addition to contributing to the strengthening of the alloy [29–31]. The effect of Zr on the mechanical and electrochemical behavior of such oxygen-added alloys has not been explored.

The β titanium alloys are known to be associated with inherent anisotropy related to their structural stability. These alloys also develop strong crystallographic texture during thermo-mechanical processing such as rolling and annealing [32–34]. As the presence of Zr affects the stability of these β alloys, the same can also change the texture in these materials. The variation of texture not only affects the mechanical properties of materials but may influence their electrochemical properties and biological response [35]. In a material of given composition, an effective route to change the crystallographic texture is by changing the strain path during the deformation processes [36]. For example, the cross-rolling process, in which the strain path is changed in between

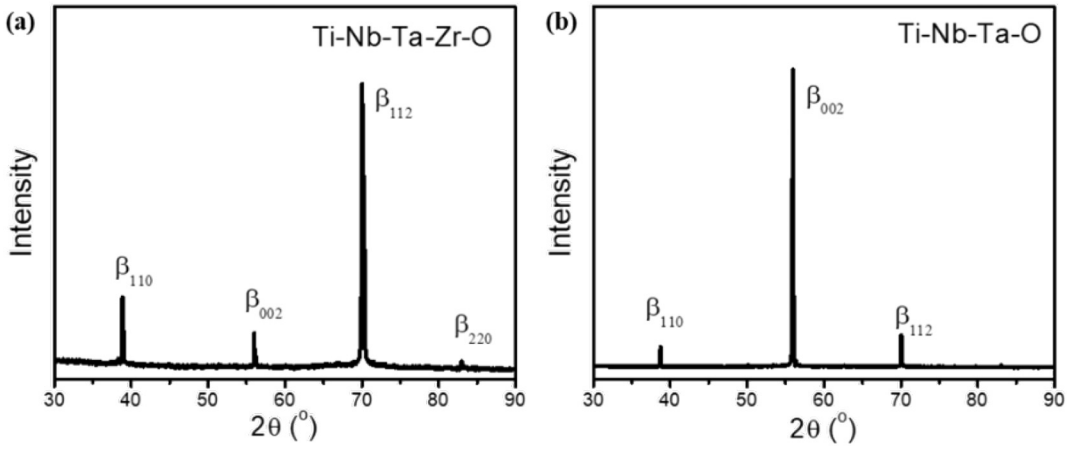

Fig. 2. X-ray diffraction patterns of the two alloys in solution treated and quenched (STQ) condition.

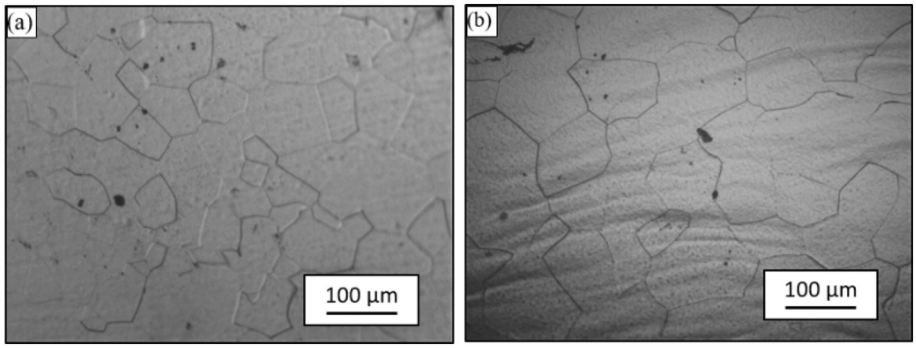

Fig. 3. Optical microstructures of STQ samples in (a) Ti-Nb-Ta-Zr-O and (b) Ti-Nb-Ta-O alloys showing equiaxed grains of the β-phase.

the rolling passes has been found to weaken the texture in several materials such as Cu-based alloys [37] whereas it has been reported to lead to a strengthening of texture for a metastable β Ti-10 V-4.5Fe-1.5Al alloy [38]. The changes in the evolution of deformation texture leads to variation in the resulting annealing texture of a material as well [39].

In the present work the effect of Zr in Ti-Nb-Ta-Zr based β alloys has been investigated. In one alloy, the composition was fixed similar to the multifunctional alloy Ti-35Nb-2Ta-3Zr-xO (wt%), which is known to exhibit attractive properties like low modulus, high strength, superelasticity and superplasticity at room temperature [7,9,40]. An identical composition was fixed in the other but without Zr. The alloys were subjected to similar processing treatments, which involved homogenization of the cast alloy followed by cold working and annealing. The cold rolling strain paths were varied in both alloys to develop different textures. The microstructure was characterized using X-ray diffraction and electron microscopy. The resultant effect on the material properties was studied by assessing the tensile properties, corrosion resistance and osteoblast attachment and proliferation.

2. Materials and methods

2.1. Material and processing

The two alloys, with compositions of Ti-34Nb-2Ta-3Zr-0.5O (wt%) and Ti-34Nb-2Ta-0.5O (wt%), were cast by vacuum arc melting using a Tungsten electrode arc furnace. The as-cast pancakes of 100 mm diameter and 12 mm thickness were homogenized in the β-field at 900 °C for 1 h and subsequently hot rolled in the same temperature to a thickness of ≈5 mm to break the as-cast microstructure. The true strain per pass during hot rolling was kept at $\varepsilon_t = 0.2$. The hot rolling process was followed by β-solutionizing at 900 °C for 0.5 h and quenching in water. These solution-treated samples (STQ) of the two alloys were cold rolled by two different modes: unidirectional rolling (UDR) and multi-step cross-rolling (MSCR). Unlike UDR, where sample direction was kept constant throughout the process, the MSCR process consisted of rotation of the samples by 90° around the normal axis after each pass (Fig. 1). The two rolling directions are taken as RD1 and RD2 and the normal direction is denoted as ND. The cold rolled samples thus obtained were further annealed at 900 °C for 0.5 h and these will be hereafter referred to as UDRA and MSCRA, respectively. All the examinations reported in following sections were carried out on the UDRA and MSCRA samples of the two alloys. Prior to hot rolling and annealing, samples were coated with Delta glaze before placing them in the furnace to prevent severe oxidation and reduce the formation of α-casing.

Table 1
Grain sizes of the STQ and annealed samples.

Material	Processing condition	Grain size Mean ± S.D. (μm)[a]
Ti-Nb-Ta-Zr-O	STQ	76 ± 32
	UDRA	52 ± 21
	MSCRA	54 ± 25
Ti-Nb-Ta-O	STQ	83 ± 34
	UDRA	48 ± 26
	MSCRA	49 ± 24

[a] n ≥ 3.

2.2. X-ray diffraction and microstructure

X-ray diffraction patterns of the samples were measured on the normal plane for each sample using Cu-Kα radiation at a scan speed of 0.011°/s in PanAnalytical X'pert Pro X-ray diffractometer. Samples for microstructural characterization were prepared by polishing the transverse cross-section (normal to RD2) up to P3000 paper followed by electropolishing at 38 V for 20 s using A3 solution in a Struers Lectropol-5 machine and etching with Kroll's reagent (2% HF, 6% HNO_3, 92% H_2O) for 30 s followed by washing in fresh water. The microstructures were examined and recorded using a light microscope (Zeiss) as well as a scanning electron microscope (ESEM, Quanta FEI).

2.3. X-ray texture and electron backscatter diffraction

The bulk texture of the different samples was measured on the normal plane by X-ray texture goniometer (Bruker D8 Discover) in Schulz reflection geometry using Co Kα radiations. Pole figures were generated for three planes, i.e., (110), (002), (112) with oscillations of the samples along X and Y directions at an amplitude of 0.5 mm and speed of 1 mm/s. These pole figures were used to calculate orientation distribution function (ODF) using the commercially available LaboTex software (LaboSoft s.c., Krakow, Poland). These ODFs were further used to generate the complete pole figures.

Electron backscatter diffraction (EBSD) measurement was performed on transverse cross-sectional planes (RD2) of UDRA and MSCRA samples from the two alloys in a Sirion FEI equipped with an EBSD detector (TexSEM Laboratories, Draper, UT) at 25 kV, 5.0 spot size, 13 mm working distance and step size of 1 μm. Preparation method of samples for EBSD measurement was similar to that of the microstructural characterization. The data obtained from EBSD scans were analyzed using commercially available TSL-OIM version 7.0 software (EDAX Inc., Mahwah, NJ).

2.4. Mechanical tests

The Young's modulus (E) values of the two alloys, both in STQ as well as annealed conditions, were determined by instrumented micro-indentation testing facility (CSM) using a Vicker's Micro-indenter. These measurements were performed on the normal planes (i.e. along thickness direction) of 7 × 7 × 1 mm^3 samples polished up to 0.05 μm alumina paste. Each sample was loaded up to a maximum load of 200 mN. The unloading curve obtained from the load-indentation plot was analyzed using the Oliver and Pharr method [41,42] to obtain the E values. The tensile properties of the samples were estimated by the uni-axial tensile tests performed on miniaturized samples of 6 mm

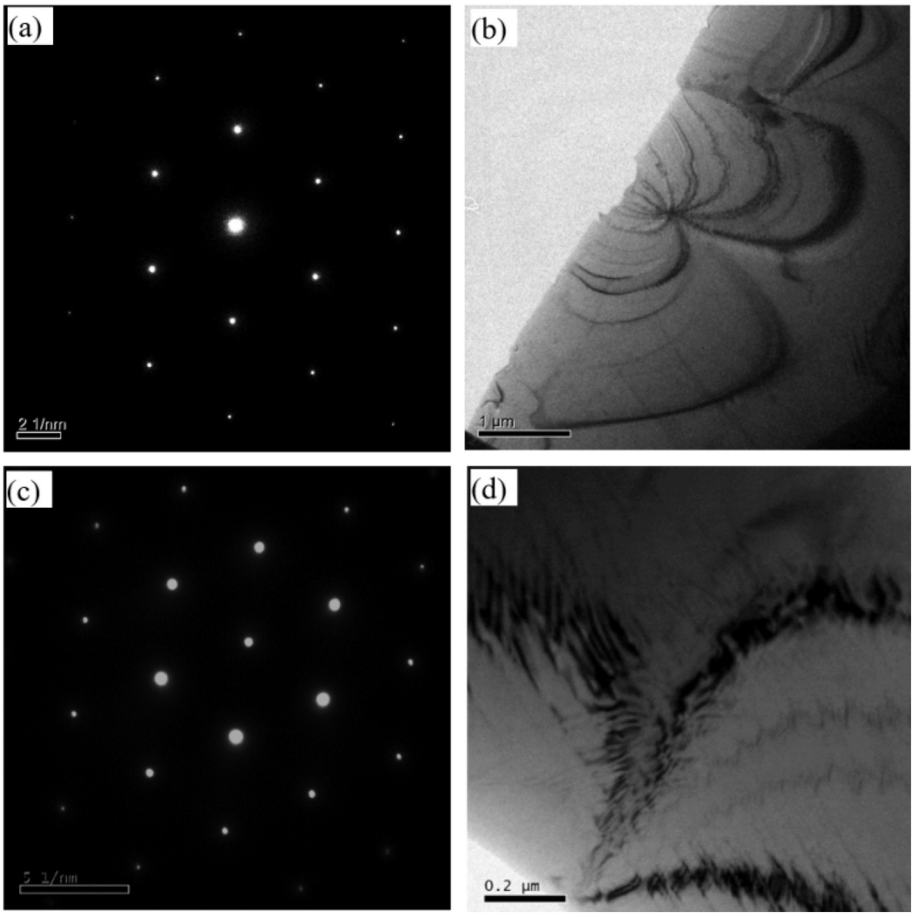

Fig. 4. (a) {111} SAD pattern, obtained from region shown in bright field TEM image (b) of STQ sample of Ti-Nb-Ta-Zr-O alloy, showing spots from only β-phase; (c) corresponding {111} pattern in Ti-Nb-Ta-O alloy showing only β-spots, captured from the bright field image in (d).

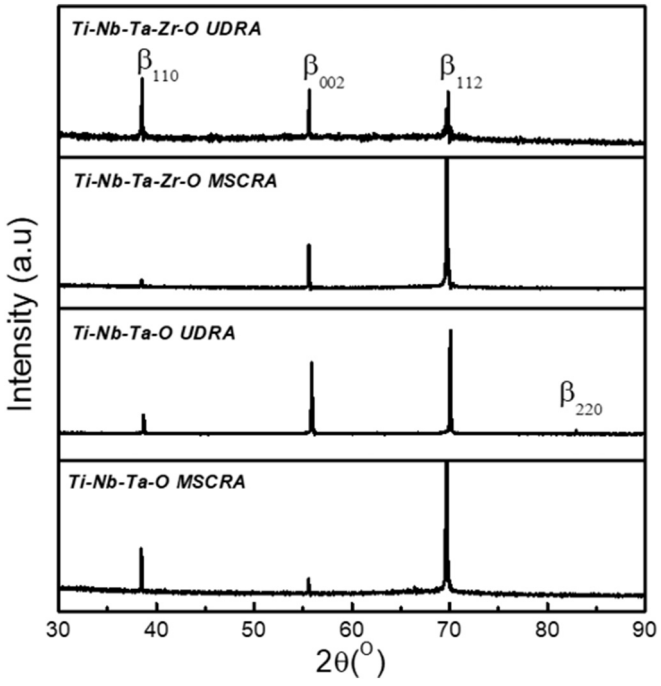

Fig. 5. X-ray diffraction patterns of samples annealed after cold rolling. The peaks are indexed as β-phase.

gauge length, 2 mm width and 0.5 mm thickness, in an Instron 5967 universal testing machine with a 5 kN load cell. The samples were cut in a manner such that tensile axis was parallel to the rolling direction (RD1 for annealed samples). These tests were performed at a strain rate of 10^{-3} s^{-1} at room temperature (~25 °C).

2.5. Electrochemical behavior

The corrosion behavior of the different samples was examined by Tafel extrapolation and impedance measurement techniques in simulated body fluid (SBF) with following composition: 8.0 g/L NaCl, 0.35 g/L $NaHCO_3$, 0.224 g/L KCl, 0.228 g/L $K_2HPO_4 \cdot 3H_2O$, 0.30 g/L $MgCl_2 \cdot 6H_2O$, 40 mL/L 1 M HCl, 0.278 g/L $CaCl_2$, 0.071 g/L Na_2SO_4, 6.0 g/L $(CH_2OH)_3CHN_2$ [43]. The samples were prepared using standard metallographic technique with final polishing up to 0.3 μm and were subjected to ultrasonic cleaning before the tests. A standard three electrode potentiostat (CHI604E, C.H. Instruments) was used with Pt as counter electrode and saturated calomel electrode (SCE) as the reference. The samples were immersed in SBF for 3 h prior to polarization in order to stabilize the rest potential (open circuit potential, OCP). The Tafel plots were measured at a scan rate of 12 mV/min within a range of −800 mV to +400 mV with respect to OCP. These plots were used to calculate the corrosion potential (E_{corr}) and corrosion current density (I_{corr}) were calculated by Tafel extrapolation technique.

2.6. Water contact angle

The measurement of static contact angle of ultrapure water (Sartorius Arium), on the sample surfaces was performed using a goniometer

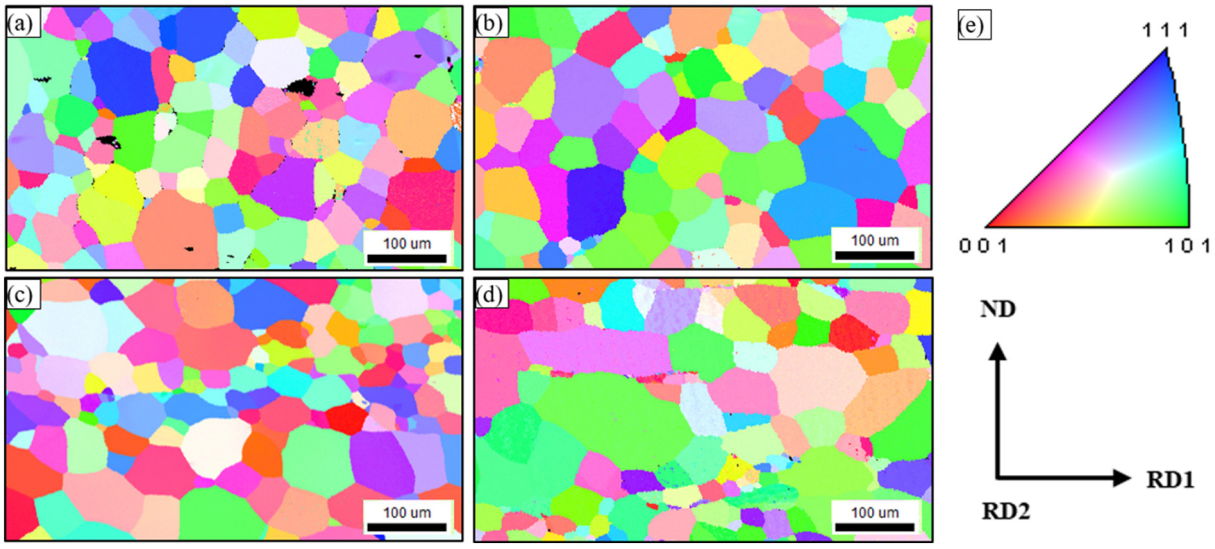

Fig. 6. IPF maps corresponding to RD2 planes, of (a) Ti-Nb-Ta-Zr-O UDRA, (b) Ti-Nb-Ta-Zr-O MSCRA, (c) Ti-Nb-Ta-O UDRA and (d) Ti-Nb-Ta-O MSCRA samples, showing strain-free equiaxed grains; the IPF color map along with reference axis system are shown in (e).

(OCA 15EC, Dataphysics). The sample surfaces were prepared using standard metallographic technique with a final polishing up to 0.3 μm. Contact angle was measured after placing 1 μL of water droplet on the sample. Three replicates of each sample were tested for statistical analysis.

2.7. Cell attachment and proliferation

For the assessment of biological performance, square-shaped samples with a cross-section of 7 mm × 7 mm were cut using the electro-discharge machine (EDM, Accutex) and then polished up to a finish of 0.3 μm. Subsequently these were sterilized by immersing in ethanol for 30 min followed by exposure to UV for 1 h. Thereafter, the samples were placed individually in wells of 48-well tissue culture polystyrene (TCPS) plate. 300 μL of cell suspension of containing 5×10^3 cells of MC3T3-E1 subclone 4 pre-osteoblast cell line (ATCC) was added to each well. The medium used for culturing the cells was α-minimum essential medium (α-MEM) supplemented with 10% (v/v) fetal bovine serum (FBS, Gibco, Life Technologies). Penicillin-streptomycin (Sigma-Aldrich) antibiotic was also added to the culture media at 1% (v/v) concentration. The cells were passaged using Trypsin-EDTA. For all the samples reported here, passage 31 cells were used. The attachment and proliferation of the cells was characterized at 1 d and 7 d after seeding, respectively. The cell viability was measured by quantification of DNA using the Picogreen assay (Invitrogen). In order to examine the cell morphology, fluorescently-labeled cells were imaged. For each time interval, six replicates (n = 6) of each sample were used for each time interval; four replicates for the assay and two for imaging. Commercially pure (CP) titanium sheets of same size were used as control. For the Picogreen assay, cells were lysed by incubating specimens in a 200 μL solution of 0.2 mg/mL proteinase K (Sigma) and 0.02% sodium dodecyl sulfate (SDS, Sigma) for 24 h at 37 °C. Subsequently, 100 μL of Picogreen working solution was added to 100 μL lysate. For imaging of the cells using fluorescence microscopy, cells were fixed using 3.7% formaldehyde at 25 °C for 30 min. These cells were subsequently permeabilized with 0.2% Triton X (Sigma Aldrich). The actin filaments were stained

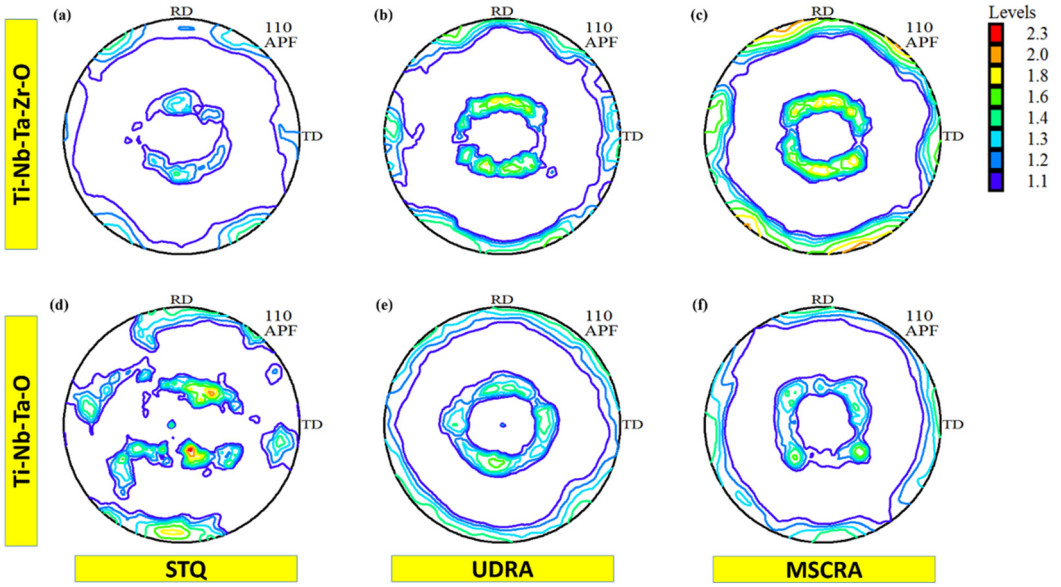

Fig. 7. (110) pole figures of all samples obtained from X-ray texture measurements: (a) Ti-Nb-Ta-Zr-O STQ, (b) Ti-Nb-Ta-Zr-O UDRA, (c) Ti-Nb-Ta-Zr-O MSCRA, (d) Ti-Nb-Ta-O STQ, (e) Ti-Nb-Ta-O UDRA and (f) Ti-Nb-Ta-O MSCRA.

using 25 μg/mL Alexa Fluor 546 (Invitrogen) at 25 °C for 15 min, whereas the cell nuclei were stained using 0.2 μg/mL DAPI (Invitrogen) at 25 °C for 5 min. Stained cells were imaged with an inverted fluorescence microscope (Olympus).

3. Results and discussion

3.1. Microstructure

The X-ray diffraction (XRD) patterns of Ti-Nb-Ta-Zr-O and Ti-Nb-Ta-O alloys after β-solutionizing and quenching (STQ) are shown in Fig. 2. Both the patterns consist of peaks from the β-phase of titanium. The microstructures of both the materials in STQ condition show equiaxed grains of the β phase (Fig. 3). The equiaxed morphology of the β grains is attributed to rolling prior to solution treatment. The grain sizes of the solution-treated samples are presented in Table 1.

In Ti-Nb-Ta-Zr based alloys with compositions, presence of the other metastable phases such as orthorhombic α″-martensite and athermal ω-phase upon quenching from β-phase has been reported in literature [26,44]. XRD patterns recorded in the present investigation do not indicate the presence of any of these phases. TEM examinations were also carried out on the STQ samples to investigate the presence of these second phases undetected by X-ray diffraction. However, the TEM images in Fig. 4 reveal only beta phases as their selected area diffraction

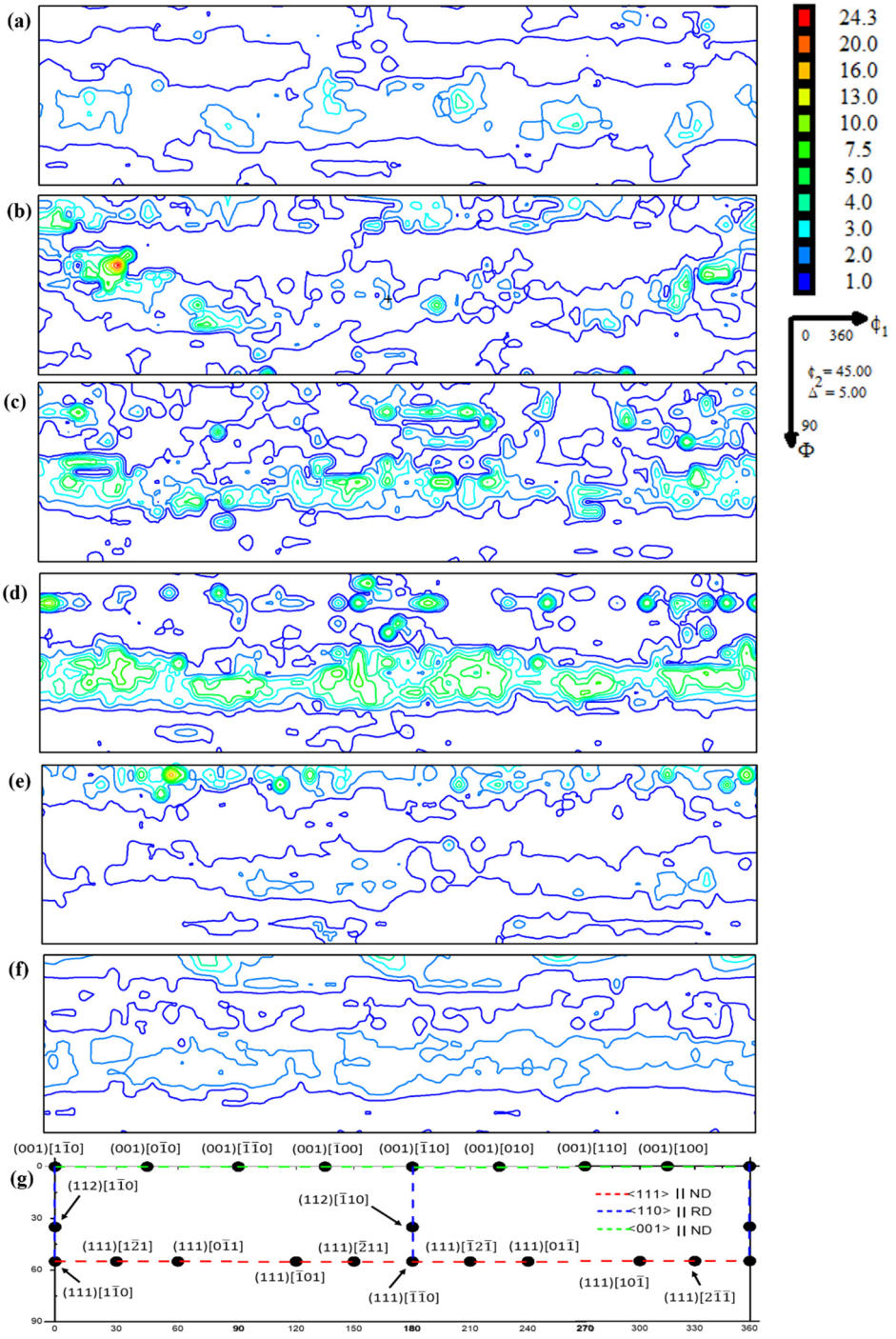

Fig. 8. ODF sections at $\varphi_2 = 45°$, of all samples obtained from X-ray texture measurements: (a) Ti-Nb-Ta-Zr-O STQ, (b) Ti-Nb-Ta-O STQ, (c) Ti-Nb-Ta-Zr-O UDRA, (d) Ti-Nb-Ta-Zr-O MSCRA, (e) Ti-Nb-Ta-O UDRA and (f) Ti-Nb-Ta-O MSCRA; g shows a schematic of ODF section at $\varphi_2 = 45°$, showing the typical components found in rolled and annealed BCC alloys.

Table 2
Volume fraction (%) of grains having {100}, {110} and {111} axes, oriented along ND-plane.

Material	Processing condition	(100)‖ND	(110)‖ND	(111)‖ND
Ti-Nb-Ta-Zr-O	STQ	7.66	6.81	21.96
	UDR	14.21	5.92	13.99
	UDRA	7.05	5.41	18.74
	MSCR	13.29	4.87	25.07
	MSCRA	6.34	4.53	23.79
Ti-Nb-Ta-O	STQ	10.29	7.53	14.45
	UDR	14.38	6.28	16.74
	UDRA	11.83	5.07	17.09
	MSCR	24.44	3.65	14.97
	MSCRA	10.71	6.58	17.35

patterns confirm. Fig. 4a and c shows {111} diffraction spots from beta phase in Ti-Nb-Ta-Zr-O and Ti-Nb-Ta-O alloys, respectively. While Fig. 4a was obtained from the region shown in Fig. 4b, Fig. 4c was obtained from the region shown in Fig. 4d. Both Fig. 4b and d indicate presence of bend contours on the thin foil. One possible reason for the absence of ω and α″ phases could be the presence of oxygen, which retards the formation of the ω and α″ phases upon quenching [45,46]. Even in Ti-Nb-Ta-O, the absence of Zr did not affect the stability of the β phase possibly due to the oxygen content.

Fig. 5 shows the XRD patterns of the differently rolled materials followed by annealing, namely, the UDRA and MSCRA samples. The XRD patterns in this case too reveal the presence of β phase alone. The sharp peaks without any broadening indicate stress-relieving and formation of defect-free grains in all the samples after annealing. However, the relative intensities between the planes are different for the two compositions as well as for the processing conditions. This difference may be attributed to the evolution of different crystallographic texture during cold working and subsequent annealing. Inverse pole figure (IPF) maps parallel to TD generated by the EBSD of the annealed samples are shown in Fig. 6. All the samples show equiaxed grains with similar grain sizes (Table 1). However, the grain sizes in these samples are lower than for the STQ samples. The STQ treatment performed to ensure stabilization of the β grains after hot rolling results in further growth of the dynamically recrystallized β grains, whereas in the cold rolled and annealed samples static recrystallization and controlled grain growth lead to finer sized grains.

3.2. Effect of processing on texture

The complete pole figures of the (110) plane, generated from the ODFs, which were derived from the experimental pole figures of the different samples are shown in Figs. 7a–f. The (110) pole figure of Ti-Nb-Ta-O alloy has overall higher intensity as compared to that of the Ti-Nb-Ta-Zr-O alloy in the STQ condition. The $\varphi_2 = 45°$ sections of the ODFs are also shown in Fig. 8a–f, along with a schematic of the typical texture fibers and components found in this corresponding section of the ODF in BCC materials (Fig. 8g). The ODFs in STQ condition, shown in Fig. 8a and b for corresponding samples, consist of clearly discernible fibers. In the ODF of the Ti-Nb-Ta-Zr-O alloy the highest intensities are observed at (111)⟨112⟩ orientations along the γ-fiber (ND‖(111)), i.e., at $\varphi = 54.7°$. In contrast, the ODF of Ti-Nb-Ta-O shows maximum intensity at (112)[0$\bar{2}$1] and (112)[110] locations. In addition, along ND‖(100) fiber ($\varphi = 0°$) and along α fiber, i.e., RD‖(110) ($\varphi_1 = 0°$), (001)[110] and (100)[0$\bar{1}$3] components were found prominent. The ODFs indicate a stronger texture in the Ti-Nb-Ta-O alloy. The components belonging to α and γ fibers have previously been reported in BCC materials as a result of hot and cold rolling [47–50].

The complete (110) pole figures of the Ti-Nb-Ta-Zr-O samples are shown in Fig. 7b and c, for UDRA and MSCRA samples respectively. While the corresponding pole figures for Ti-Nb-Ta-O alloy are shown in Fig. 7e and f, respectively. The pole figures of annealed samples are represented following the pole figures of STQ samples, which denote standard rolling direction and transverse direction (TD) as RD1 and RD2, respectively, for both UDRA and MSCRA samples. The ODFs corresponding to these samples at $\varphi_2 = 45$ are also shown in Fig. 8c, d, e and f, respectively. As the ODF plots indicate presence of components along or near to ND‖⟨111⟩ and ND‖⟨001⟩ fiber, therefore, the volume fractions of the grains having (001) and (111) planes parallel to the normal plane, in annealed (UDRA and MSCRA) conditions are summarized in Table 2. The volume fractions of the ND‖⟨110⟩ grains are also included as (110) planes are the closest-packed plane in BCC alloys. For easy understanding of the texture evolution from the STQ to the annealed condition through cold rolling, the volume fraction of the texture components in STQ, UDR (unidirectional cold rolling after STQ) and MSCR (multi-step cross rolling after STQ) conditions are also included in Table 2. In Ti-Nb-Ta-Zr-O, UDRA and MSCRA show nearly similar texture with ND‖⟨111⟩ fiber being comparatively stronger than the ND‖⟨001⟩ fiber. However, the evolution of texture components along these two fibers show different trend. The ND‖⟨001⟩ components strengthen during rolling of STQ (both UDR and MSCR) and then during annealing reduce to the similar level as STQ. The ND‖⟨111⟩ grains, on the other hand, decrease during UDR and strengthen in UDRA. Cross-rolling, however, leads to an increase in the strength of ND‖⟨111⟩ fiber and though subsequent annealing reduces the intensity, the decrease is lesser as compared to the ND‖⟨001⟩ grains.

In Ti-Nb-Ta-O alloy, a similar trend can be noticed while analyzing the strength of the two aforementioned fibers. Here too, rolling led to an increase in the strength of components along ND‖⟨001⟩ fiber, which is significant in MSCR, in particular. A weakening of these components takes place during annealing. The intensity of ND‖⟨111⟩ fiber, however, does not vary much during cold rolling and shows a tendency to strengthen during annealing. This strengthening of γ-oriented grains during annealing, can be attributed to the preferential recrystallization of these grains due to their higher stored energy [38,51]. An overall comparison between texture evolution in the two alloys indicates higher fraction of grains acquire ND‖⟨111⟩ orientations in Ti-Nb-Ta-Zr-O, whereas more grains develop ND‖⟨001⟩ orientation in Ti-Nb-Ta-O. This is concurrent with their volume fractions in STQ.

Table 3
Elastic moduli of the two alloys in different conditions.

Material	Processing condition	E (GPa)[a]
Ti-Nb-Ta-Zr-O	STQ	68 ± 2
	UDRA	66 ± 3
	MSCRA	67 ± 3
Ti-Nb-Ta-O	STQ	63 ± 3
	UDRA	64 ± 4
	MSCRA	64 ± 3

[a] Mean ± S.D. for n ≥ 10.

3.3. Elastic modulus

The average Young's modulus values of the Ti-Nb-Ta-Zr-O and Ti-Nb-Ta-O in all the conditions are summarized in Table 3. After β-solution treatment, the E values were found to be 68 ± 2 GPa and 63 ± 3 GPa, respectively, in STQ condition. After annealing, the Ti-Nb-Ta-Zr-O alloy showed values of 66 ± 3 GPa (UDRA), 67 ± 3 GPa (MSCRA), whereas the corresponding values for Ti-Nb-Ta-O alloy are 64 ± 4 GPa and 64 ± 3 GPa, respectively. These values are well in accordance with the values reported for similar structures by previous investigators [4,16,21,52,53]. It can also be noted that Ti-Nb-Ta-O alloy shows a marginally lower modulus as compared to the Ti-Nb-Ta-Zr-O. This may be attributed to the composition as well as the crystallographic textures of the two alloys. It is well known that the E values of these alloys depend upon the stability of the β-phase. Though β has lower E value than α or ω phases, its modulus increases as it becomes more stable

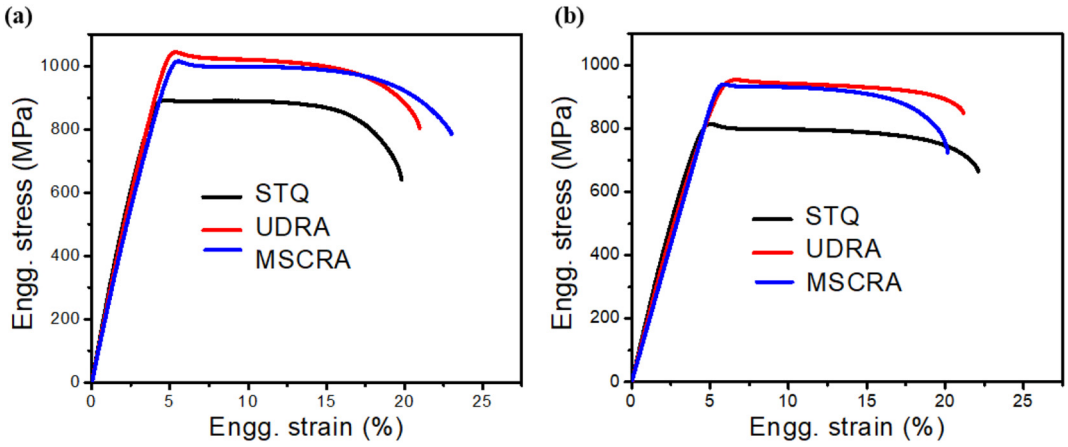

Fig. 9. Engineering stress-strain curves obtained from tensile tests of (a) Ti-Nb-Ta-Zr-O and (b) Ti-Nb-Ta-O alloys.

[5]. In the present case, the composition of the two alloys varies only in terms of the Zr-content. As Zr does not affect the stability of the beta phase and its e/a ratio is also same as that of Ti, it should not affect the modulus of the β-phase. However, the presence of Zr in Ti-Nb-Ta-Zr-O alloy modifies the texture, as discussed in the previous section. The BCC Ti structure of β due to its anisotropy shows different elastic response in different crystallographic axes with $E_{\langle 001\rangle} < E_{\langle 011\rangle} < E_{\langle 111\rangle}$. The slightly higher values of elastic modulus in Ti-Nb-Ta-Zr-O may be caused by its higher percentage of ND ∥ ⟨111⟩ oriented grains. For a given alloy, among the different conditions (STQ, UDRA and MSCRA) the difference of crystallographic texture is much lesser. Therefore the Young's modulus does not vary much between STQ and differently annealed conditions. This may possibly be due to the presence of only stabilized β-phase in all conditions. The moduli for all the samples have small standard deviation associated with them; the uniformity in the microstructure and weak textures may be attributed for this. However, considering the grain size of the sample, the effect of grain orientation may affect the micro-indentation modulus because of its smaller scale.

3.4. Tensile properties of the alloys

Representative plots of engineering stress-strain curves obtained from tensile tests of Ti-Nb-Ta-Zr-O and Ti-Nb-Ta-O alloys are shown in Fig. 9a and b. The yield strength, ultimate tensile strength and percentage elongation (to fracture) values are summarized in Table 4. The tensile plots of both the alloys look similar in STQ, UDRA and MSCRA conditions showing considerable plastic deformation after yielding. The two alloys show higher yield and tensile strength values after annealing than in STQ conditions. As both the alloys show similar microstructure in STQ and annealed conditions, the higher strength in the annealed samples can be attributed to their lower grain sizes. Strength values in annealed samples look similar for UDRA and MSCRA. In all the conditions, Ti-Nb-Ta-Zr-O shows higher strength than Ti-Nb-Ta-O, which can be attributed to solid solution strengthening effect of Zr [54]. Presence of Zr also causes texture variation, though the effect of texture on the strength values was much lesser as can be seen from the comparison of strength values of UDRA and MSCRA samples in both alloys (Table 4). The ductility values for the different conditions are similar.

In literature, yield and tensile strength values have been reported for several Ti-Nb based materials with a β-only microstructure in solution treated or annealed [4,27,55–60]. A comparison of the reported strength values with the present alloys suggests that the hardness achieved by the present alloys are similar to only those with a substantial amount of oxygen present (>0.3 wt%) or in them [56,61]. Wei et al. [57] studied the effect of oxygen on mechanical properties of Ti-22Nb-0.7Ta-2Zr alloy, a composition similar to the Ti-Nb-Ta-Zr-O alloy in the present investigation, and reported significant increase in strength with the addition of oxygen. The alloy studied by Qazi et al. [56], showed comparatively higher strength than the present alloy, though it also contained Ta and Zr in higher level (5% and 7%, respectively) The alloys where oxygen content was lower, the strength obtained was also significantly lower [55,59]. Therefore, the hardness achieved by the β microstructures in the present materials can primarily be attributed to the interstitial strengthening effect of oxygen. This strength is further improved by the refining the grain size by cold rolling and annealing as

Table 4
Tensile properties of the two alloys in different conditions.

Material	Processing condition	Yield strength[a] (MPa)	Ultimate tensile[a] strength (MPa)	Elongation[a] (%)
Ti-Nb-Ta-Zr-O	STQ	766 ± 31	908 ± 24	20 ± 2.5
	UDRA	842 ± 22	987 ± 30	22 ± 5.0
	MSCRA	876 ± 33	1006 ± 38	23 ± 0.8
Ti-Nb-Ta-O	STQ	693 ± 16	840 ± 14	19 ± 2.3
	UDRA	795 ± 8	923 ± 7	21 ± 2.9
	MSCRA	810 ± 22	945 ± 14	20 ± 2.3

[a] Mean ± S.D. for n ≥ 3.

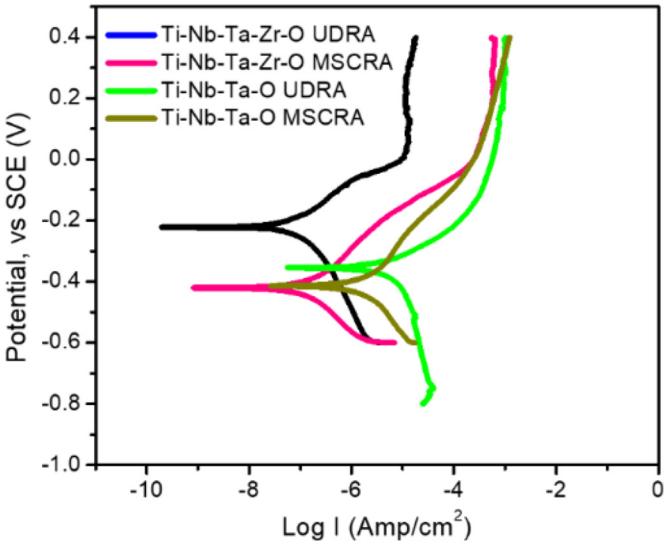

Fig. 10. Tafel plots for the two alloys in the annealed condition showing lower corrosion current densities for the Ti-Nb-Ta-Zr-O samples.

Table 5
Electrochemical properties of the two alloys.

Material	Processing condition	Corrosion current density I_{corr} ($\mu A/cm^2$)[a]	Corrosion potential E_{corr} (V vs SCE)[a]
Ti-Nb-Ta-Zr-O	UDRA	0.11 ± 0.01	−0.19 ± 0.01
	MSCRA	0.26 ± 0.14	−0.37 ± 0.07
Ti-Nb-Ta-O	UDRA	4.15 ± 1.44	−0.31 ± 0.06
	MSCRA	1.98 ± 0.42	−0.41 ± 0.01

[a] Mean ± S.D. for n ≥ 3.

well as the presence of Zr. Although the absence of Zr in the Ti-Nb-Ta-O alloy leads to a decrease in strength, this alloy shows a strength value which is comparable to that of other Ti-based orthopedic materials which lies mostly in the range of (~900–1000 MPa). The effect of oxygen on tensile properties becomes more pronounced when the ductility values of the present alloys are compared with Ti-Nb based similar β-alloys. The ductility of the two alloys in all conditions is lower than the ones reported in some literature for alloys with very low oxygen content [4,9,52]. However, as oxygen content increases, the ductility gets affected [9,57].

3.5. Electrochemical behavior

Fig. 10 shows the Tafel plots of UDRA and MSCRA samples of the two alloys. The Tafel plots are similar in nature across composition and crystallographic texture. The average values of exchange current density (I_{corr}) and corrosion potential (E_{corr}) obtained from the different samples are summarized in Table 5. The Ti-Nb-Ta-Zr-O shows a lower I_{corr} value as compared to Ti-Nb-Ta-O indicating higher rate of corrosion in Ti-Nb-Ta-O. The presence of Zr in Ti-Nb-Ta-Zr-O improves its corrosion rate by improving the strength of the oxide films [27,28].

In Ti-Nb-Ta-Zr-O, the corrosion rate of UDRA sample is marginally lower than MSCRA, whereas for Ti-Nb-Ta-O, UDRA shows higher corrosion rate than MSCRA. The surface energy of a material is known to be a key parameter that affects corrosion rate of a material. Again, for a single-phase polycrystalline material, surface energy is primarily a function of the grain size, grain boundary energy, individual orientation of each crystal or grain and defects within the grains. With both the alloys showing defect-free recrystallized grains of similar sizes in UDRA and MSCRA samples, the crystallographic texture is the only variable in between these two processing conditions is the of the materials. The surface energy of a crystal increases with decreasing atomic density of the surface. Therefore, the surface having more closest-packed planes will have lower surface energy than the one having more loose-packed planes [35,62]. In BCC materials, the closest packed planes are (110) with an atomic density of ~$1.41/a^2$ per unit cell where 'a' is the lattice parameter of a BCC unit cell. Apart from this plane, the (100) plane and (111) planes have atomic densities of $1/a^2$ and $0.577/a^2$. A comparison between the volume fractions of grains having normal planes parallel to these three planes in Table 3 shows that the overall number of ND∥(110) grains is less in all samples compared to the ND∥(100) and ND∥(111). In Ti-Nb-Ta-Zr-O, UDRA has higher number of both {110} and {100} grains, but lower number of {111} grains. The lower corrosion rate in UDRA than MSCRA in Ti-Nb-Ta-ZR-O seems a direct consequence of this. For Ti-Nb-Ta-O alloy, the normal plane in UDRA is parallel to more (100) planes but less (110) and (111) grains. Here, the higher corrosion rate in UDRA can be caused by the lesser number of (110) planes, which helps to helps to overcome the advantage of higher number of (111) planes. Therefore, having (110) planes on the surface may be more advantageous in BCC system for electrochemical properties. Again, the corrosion results only imply the importance of composition though crystallographic texture is thus found to affect the overall corrosion rate of the two materials.

Table 6
Water contact angles for the different samples.

Material	Processing condition	Water contact angle (θ°)[a]
cp-Ti	Hot rolled	73 ± 3.0
Ti-Nb-Ta-Zr-O	UDRA	75 ± 1.4
	MSCRA	77 ± 1.6
Ti-Nb-Ta-O	UDRA	80 ± 2.2
	MSCRA	78 ± 2.1

[a] Mean ± S.D. for n ≥ 3.

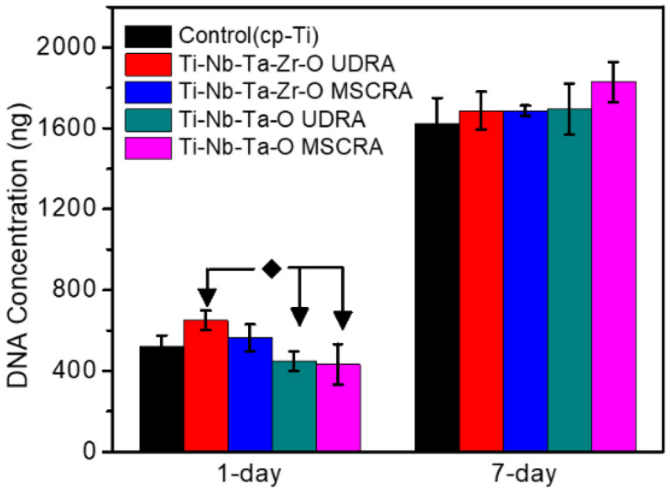

Fig. 11. DNA concentrations of osteoblast cells at days 1 and 7; ♦ indicates statistically significant ($p < 0.05$) differences.

3.6. Surface energy

The average values of the water contact angles (θ) of the four annealed samples are summarized in Table 6 along with that of the cp-Ti. In Ti-Nb-Ta-Zr-O, the contact angles are 75 ± 1.4° and 77 ± 1.6° for UDRA and MSCRA, respectively. The slightly higher contact angle in MSCRA be associated with its higher number of (111) planes. The absence of Zr also results in a small increase in the contact angle in Ti-Nb-Ta-O with it showing values of 80 ± 2.2° for UDRA and 78 ± 2.1° for MSCRA. The slightly higher value of UDRA can result from the presence of lesser number of (110) planes on ND as compared to MSCRA. In BCC, the (100) planes are more-closely packed than (111). The contact angle for cp-Ti was also measured for comparison and was found to be 73 ± 3.0. The contact angle, which is a measure of the surface energy of a material, indicates that the surface energy of the two alloys is affected by presence of alloying elements and composition. For both alloys, presence of higher surface energy planes leads to an overall increase, although minor, in the water contact angle.

3.7. Biological behavior

The average values of the DNA content for the mouse pre-osteoblasts at 1 d and 7 d are plotted in Fig. 11. In both alloys, the average DNA content is found to be similar to that of cp-Ti, which suggests that the surfaces of the alloys are conducive for the attachment of the bone cells. The DNA content increases by 7 d from 1 d for all the samples indicating comparable proliferation rate for the β alloys with respect to cp-Ti. Representative fluorescence images of the cells shown in Fig. 12 clearly depict the difference in the number of cells between 1 d and 7 d for all samples. However, for a given time point, the number of cells appear similar. The Ti-Nb-Ta-Zr-O, particularly in the UDRA condition, shows higher cell attachment than both UDRA and MSCRA samples in of Ti-Nb-Ta-O alloy. This may be caused by the lower surface energy of the former samples as compared to the Ti-Nb-Ta-Zr-O samples (Table 6). Overall, the biological characterizations indicate that the

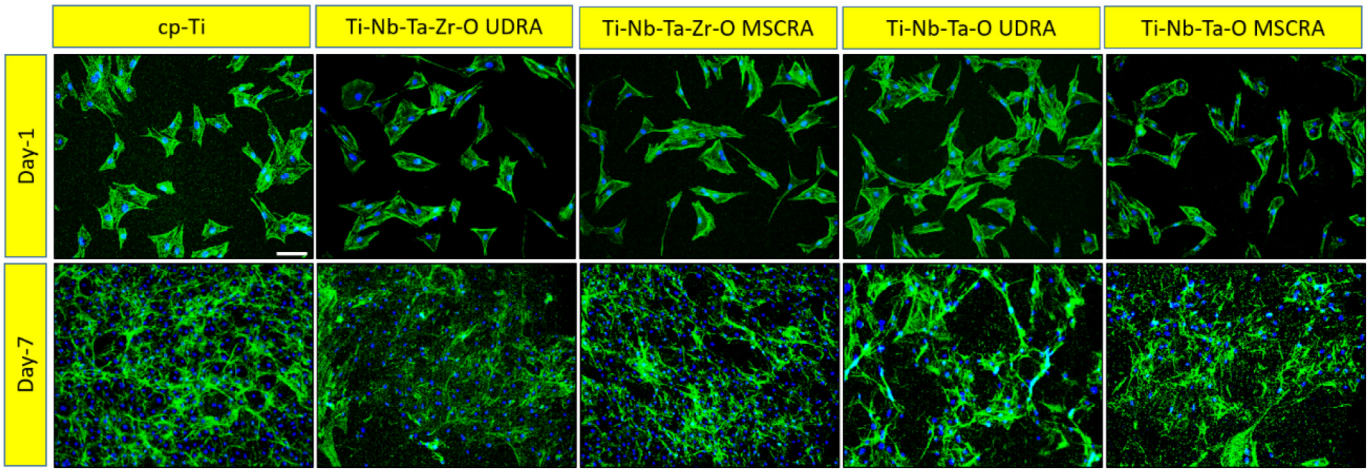

Fig. 12. Fluorescence micrographs of osteoblast cells showing attachment at days 1 and 7; the blue and green colors represent nucleus and F-actin, respectively. Scale bar = 100 μm. (For interpretation of the references to color in this figure legend, the reader is referred to the web version of this article.)

biological performances are comparable across composition and processing conditions and are as good as that of the cp-Ti [63].

4. Conclusion

In the present study, the effect of composition and texture on the mechanical and functional properties of two β titanium alloys has been studied. The major findings of this work are as follows:

(1) In both Ti-Nb-Ta-Zr-O and Ti-Nb-Ta-O alloys, the β phase was stabilized at room temperature in solution treated as well as annealed condition. This was particularly significant for Ti-Nb-Ta-O alloy, as the absence of Zr did not affect the stability of the β phase due to sufficient amount of oxygen present in the alloys.
(2) The crystallographic textures were found to be different for the two alloys. While in Ti-Nb-Ta-Zr-O, texture was dominated by the components along the ND∥⟨111⟩ fiber, the texture of Ti-Nb-Ta-O showed the presence of components along ND∥⟨111⟩ fiber. The variation in textures of the annealed samples was primarily affected by their rolling texture evolution. The changes in the strain path also affected the texture in the two alloys.
(3) The presence of only β-phase in the two alloys resulted in low modulus values for both alloys. The presence of Zr, however, led to a slight increase in the modulus in Ti-Nb-Ta-Zr-O alloy, by causing formation of higher number of ND∥⟨111⟩ oriented grains in β-phase. The two alloys show high tensile strength primarily due to the interstitial strengthening effect of oxygen. Whereas both solution treated as well as annealed materials have similar microstructure, the strength was higher in annealed materials due to reduction in the grain size. The strength of the Ti-Nb-Ta-Zr-O alloy was found to be higher in all conditions than that of the corresponding Ti-Nb-Ta-O alloy, due to solid solution strengthening effect of Zr.
(4) The presence of Zr in Ti-Nb-Ta-Zr-O alloy resulted in improved corrosion resistance than that of Ti-Nb-Ta-O alloy. The effect of the resultant textures in the two alloys were also evident on corrosion resistance with the presence of higher amount of closed-packed planes leading to increased corrosion resistance.
(5) The biological behavior of the two alloys were found to depend of composition as well as crystallographic textures, as the samples with lower surface energy was found to show higher osteoblast attachment. The attachment and proliferation of both alloys were also comparable to that of the cp-Ti.

CRediT authorship contribution statement

Srijan Acharya: Conceptualization, Data curation, Formal analysis, Investigation, Methodology, Writing - original draft. **Arpana Gopi Panicker:** Data curation, Formal analysis, Investigation, Methodology. **Devara Vijaya Laxmi:** Data curation, Formal analysis, Investigation, Methodology. **Satyam Suwas:** Conceptualization, Formal analysis, Funding acquisition, Methodology, Resources, Supervision, Writing - review & editing. **Kaushik Chatterjee:** Conceptualization, Formal analysis, Funding acquisition, Methodology, Project administration, Resources, Supervision, Writing - review & editing.

Acknowledgement

The authors acknowledge the Department of Science and Technology (DST-SERB), India for funding this work.

References

[1] M. Geetha, A. Singh, R. Asokamani, A. Gogia, Prog. Mater. Sci. 54 (2009) 397–425.
[2] H. Attar, M. Bönisch, M. Calin, L.-C. Zhang, S. Scudino, J. Eckert, Acta Mater. 76 (2014) 13–22.
[3] H. Attar, M. Calin, L. Zhang, S. Scudino, J. Eckert, Mater. Sci. Eng. A 593 (2014) 170–177.
[4] S. Bahl, A.S. Krishnamurthy, S. Suwas, K. Chatterjee, Mater. Des. 126 (2017) 226–237.
[5] H. Ikehata, N. Nagasako, T. Furuta, A. Fukumoto, K. Miwa, T. Saito, Phys. Rev. B 70 (2004), 174113. .
[6] D. Kuroda, M. Niinomi, M. Morinaga, Y. Kato, T. Yashiro, Mater. Sci. Eng. A 243 (1998) 244–249.
[7] T. Saito, T. Furuta, J.-H. Hwang, S. Kuramoto, K. Nishino, N. Suzuki, R. Chen, A. Yamada, K. Ito, Y. Seno, Science 300 (2003) 464–467.
[8] X. Zhao, M. Niinomi, M. Nakai, J. Hieda, Acta Biomater. 8 (2012) 1990–1997.
[9] M. Besse, P. Castany, T. Gloriant, Acta Mater. 59 (2011) 5982–5988.
[10] D. Raducanu, V.D. Cojocaru, A. Nocivin, D.M. Gordin, I. Cinca, Mater. Sci. Eng. A 689 (2017) 25–33.
[11] I.V. Okulov, M. Bönisch, A.V. Okulov, A.S. Volegov, H. Attar, S. Ehtemam-Haghighi, M. Calin, Z. Wang, A. Hohenwarter, I. Kaban, K.G. Prashanth, J. Eckert, Mater. Sci. Eng. A 733 (2018) 80–86.
[12] M.R. Dal Bó, C.A. Salvador, M.G. Mello, D.D. Lima, G.A. Faria, A.J. Ramirez, R. Caram, Mater. Des. 160 (2018) 1186–1195.
[13] S. Bahl, S. Das, S. Suwas, K. Chatterjee, J. Mech. Behav. Biomed. Mater. 78 (2018) 124–133.
[14] P. Laheurte, F. Prima, A. Eberhardt, T. Gloriant, M. Wary, E. Patoor, J. Mech. Behav. Biomed. Mater. 3 (2010) 565–573.
[15] M. Ikeda, S.-Y. Komatsu, I. Sowa, M. Niinomi, Metall. Mater. Trans. A 33 (2002) 487–493.
[16] Y. Hao, R. Yang, M. Niinomi, D. Kuroda, Y. Zhou, K. Fukunaga, A. Suzuki, Metall. Mater. Trans. A 34 (2003) 1007–1012.
[17] M. Long, R. Crooks, H. Rack, Acta Mater. 47 (1999) 661–669.
[18] D. Raabe, B. Sander, M. Friák, D. Ma, J. Neugebauer, Acta Mater. 55 (2007) 4475–4487.

[19] V. Cojocaru, D. Raducanu, T. Gloriant, D. Gordin, I. Cinca, Mater. Sci. Eng. A 586 (2013) 1–10.
[20] S. Kuramoto, T. Furuta, J. Hwang, K. Nishino, T. Saito, Metall. Mater. Trans. A 37 (2006) 657–662.
[21] M. Tane, T. Nakano, S. Kuramoto, M. Hara, M. Niinomi, N. Takesue, T. Yano, H. Nakajima, Acta Mater. 59 (2011) 6975–6988.
[22] L. Wang, L. Xie, Y. Lv, L.-C. Zhang, L. Chen, Q. Meng, J. Qu, D. Zhang, W. Lu, Acta Mater. 131 (2017) 499–510.
[23] R. Banerjee, S. Nag, H. Fraser, Mater. Sci. Eng. C 25 (2005) 282–289.
[24] Y. Abd-elrhman, M.A.-H. Gepreel, A. Abdel-Moniem, S. Kobayashi, Mater. Des. 97 (2016) 445–453.
[25] S. Ehtemam-Haghighi, K. Prashanth, H. Attar, A.K. Chaubey, G. Cao, L. Zhang, Mater. Des. 111 (2016) 592–599.
[26] M. Abdel-Hady, H. Fuwa, K. Hinoshita, H. Kimura, Y. Shinzato, M. Morinaga, Scr. Mater. 57 (2007) 1000–1003.
[27] J. Málek, F. Hnilica, J. Veselý, B. Smola, K. Kolařík, J. Fojt, M. Vlach, V. Kodetová, Mater. Sci. Eng. A 675 (2016) 1–10.
[28] M. Geetha, U.K. Mudali, A. Gogia, R. Asokamani, B. Raj, Corros. Sci. 46 (2004) 877–892.
[29] T. Furuta, S. Kuramoto, J. Hwang, K. Nishino, T. Saito, M. Niinomi, Mater. Trans. 48 (2007) 1124–1130.
[30] H.-p. Duan, H.-x. Xu, W.-h. Su, Y.-b. Ke, Z.-q. Liu, H.-h. Song, Int. J. Miner. Metall. Mater. 19 (2012) 1128–1133.
[31] X. Min, P. Bai, S. Emura, C. Cheng, B. Jiang, K. Tsuchiya, Mater. Sci. Eng. A 684 (2017) 534–541.
[32] M.A.-H. Gepreel, Texturing tendency in β-type Ti-alloys, Recent Developments in the Study of Recrystallization, InTech, 2013.
[33] B. Sander, D. Raabe, Mater. Sci. Eng. A 479 (2008) 236–247.
[34] W. Guo, H. Xing, J. Sun, X. Li, J. Wu, R. Chen, Metall. Mater. Trans. A 39 (2008) 672–678.
[35] S. Bahl, S. Suwas, K. Chatterjee, RSC Adv. 4 (2014) 38078–38087.
[36] S. Suwas, A. Singh, K.N. Rao, T. Singh, Z. Met. 93 (2002) 918–927.
[37] S. Suwas, A. Singh, Mater. Sci. Eng. A 356 (2003) 368–371.
[38] N.P. Gurao, S. Suwas, Mater. Sci. Eng. A 504 (2009) 24–35.
[39] S. Suwas, A. Singh, K.N. Rao, T. Singh, Z. Met. 94 (2003) 1313–1319.
[40] N. Nagasako, R. Asahi, D. Isheim, D.N. Seidman, S. Kuramoto, T. Furuta, Acta Mater. 105 (2016) 347–354.
[41] W.C. Oliver, G.M. Pharr, J. Mater. Res. 7 (1992) 1564–1583.
[42] W.C. Oliver, G.M. Pharr, J. Mater. Res. 19 (2004) 3–20.
[43] S. Bahl, S. Raj, S. Vanamali, S. Suwas, K. Chatterjee, Mater. Technol. 29 (2013) B64–B68.
[44] X. Tang, T. Ahmed, H. Rack, J. Mater. Sci. 35 (2000) 1805–1811.
[45] N. Paton, J. Williams, Scr. Metall. 7 (1973) 647–649.
[46] J. Williams, B. Hickman, D. Leslie, Metall. Trans. A. 2 (1971) 477–484.
[47] S. Suwas, R. Ray, A. Singh, S. Bhargava, Acta Mater. 47 (1999) 4585–4598.
[48] S. Suwas, R. Ray, Metall. Mater. Trans. A 31 (2000) 2339–2350.
[49] N. Gey, M. Humbert, M. Philippe, Y. Combres, Mater. Sci. Eng. A 219 (1996) 80–88.
[50] C. Lan, Y. Wu, L. Guo, H. Chen, F. Chen, J. Mater. Sci. Technol. 34 (2018) 788–792.
[51] A. Helth, S. Pilz, T. Kirsten, L. Giebeler, J. Freudenberger, M. Calin, J. Eckert, A. Gebert, J. Mech. Behav. Biomed. Mater. 65 (2017) 137–150.
[52] A. Panigrahi, B. Sulkowski, T. Waitz, K. Ozaltin, W. Chrominski, A. Pukenas, J. Horky, M. Lewandowska, W. Skrotzki, M. Zehetbauer, J. Mech. Behav. Biomed. Mater. 62 (2016) 93–105.
[53] H. Rack, J. Qazi, Mater. Sci. Eng. C 26 (2006) 1269–1277.
[54] Y. Zhou, Y. Li, X. Yang, Z. Cui, S. Zhu, J. Alloys Compd. 486 (2009) 628–632.
[55] S. Bahl, A. Devadiga, K. Chatterjee, S. Suwas, Proceedings of the 13th World Conference on Titanium, Wiley Online Library, 2016 935–938.
[56] J. Qazi, H. Rack, B. Marquardt, JOM 56 (2004) 49–51.
[57] Q. Wei, L. Wang, Y. Fu, J. Qin, W. Lu, D. Zhang, Mater. Des. 32 (2011) 2934–2939.
[58] A. Ramarolahy, P. Castany, F. Prima, P. Laheurte, I. Péron, T. Gloriant, J. Mech. Behav. Biomed. Mater. 9 (2012) 83–90.
[59] M. Abdel-Hady, K. Hinoshita, H. Fuwa, Y. Murata, M. Morinaga, Mater. Sci. Eng. A 480 (2008) 167–174.
[60] J. Stráský, P. Harcuba, K. Václavová, K. Horváth, M. Landa, O. Srba, M. Janeček, J. Mech. Behav. Biomed. Mater. 71 (2017) 329–336.
[61] T. Furuta, S. Kuramoto, J. Hwang, K. Nishino, T. Saito, Mater. Trans. 46 (2005) 3001–3007.
[62] M. Hoseini, A. Shahryari, S. Omanovic, J.A. Szpunar, Corros. Sci. 51 (2009) 3064–3067.
[63] A. Biesiekierski, J. Lin, Y. Li, D. Ping, Y. Yamabe-Mitarai, C. Wen, Acta Biomater. 32 (2016) 336–347.